

¹ Space-Time Ambiguity Function for ² Electronically Scanned ISR

John Swoboda,¹ Joshua Semeter,¹ Philip Erickson²

Corresponding author: J. P. Swoboda, Department of Electrical & Computer Engineering,
Boston University, 8 Saint Marys Street Boston, MA 02215, USA. (swoboj@bu.edu)

¹Department of Electrical & Computer
Engineering, Boston University, Boston,
Massachusetts, USA.

²Atmospheric Science Division, MIT
Haystack Observatory, Westford
Massachusetts, USA.

Electronically steerable array (ESA) technology has recently been used in incoherent scatter radars (ISR). These arrays allow for pulse-to-pulse steering of the antenna beam as opposed to a dish antenna which can only measure plasma parameters along one beam at a time. This allows for more flexibility in the measurement of ionospheric plasma parameters.

Currently these systems are operating in the high latitude region where the ionosphere is highly dynamic in both space and time. Because of the highly dynamic nature of the ionosphere in this region it is important to differentiate between artifacts and the true behavior of the plasma. Often the three dimensional data is fitted in a spherical coordinate space and then the parameters are interpolated to a Cartesian grid. This and other sources of error could be impacting the reconstructions of the plasma parameters.

To take advantage of the new flexibility of ESA system we present a new way of analyzing ISR through use of the space-time ambiguity function. This concept is similar to the range ambiguity function that is used in traditional ISR for scanning antenna systems but has been extended to all spatial dimensions along with time as well.

The use of this new ambiguity function allow us to pose this problem in terms of a linear inverse problem for the lags of the intrinsic plasma autocorrelation function. From this we can explore the impact of non-stationarity in the plasma parameters in both time and space. Along with showing possible artifacts we will begin to explore ways of reducing these artifacts.

1. Introduction

Incoherent scatter radar (ISR) is a powerful tool for exploring the ionosphere. These systems can give measurements of electron density N_e , ion temperature T_i , electron temperature T_e , ion velocity V_i and other plasma parameters [Dougherty and Farley, 1960; Farley et al., 1961; Dougherty and Farley, 1963; Hagfors, 1961]. These parameters are measured by fitting a nonlinear theoretic autocorrelation function (ACF) model derived from first principles physics to an estimated time autocorrelation or, alternatively, the power spectrum of the scattered radar signal [Lehtinen and Huuskonen, 1996].

In order to get an estimate of the ACF with reasonable statistical properties numerous pulses have to be averaged together. With traditional dish antennas the ISR system would build these statistics in a limited number of ways. One method consists of pointing the radar beam in a specific direction and hold it there until enough pulses were integrated to get the desired statistics. Alternatively, the beam could be scanned through a field of view and collect pulses while moving. These techniques have an implicit assumptions about the stationarity of the plasma parameters. The first method assumes a stationarity in time while the pulses are collected while the second technique assumes that the velocity of the plasma is known and the beam is scanning along it's velocity or more simply that the plasma parameters are not changing along the motion of the beam.

In many cases, especially in the high latitude ionosphere, these stationarity assumptions are not met. Phenomena such as polar cap patches that may be moving

through the field of view at very high speeds and may only be within the beam for a short period of time [Dahlgren *et al.*, 2012a]. Poleward Boundary intensifications also can break these assumptions due to the two dimensional structure [Zesta *et al.*, 2006, 2002].

Recently electronically scannable array (ESA) technology has started to be leveraged by ISR community. The Advance Modular Incoherent Scatter Radar (AMISR) systems have already been deployed both at the Poker Flat Alaska (PFISR) and Resolute Bay Canada (RISR) [ami, 2014]. The EISCAT-3D project is currently being developed using phased array technology as well and will be capable of multistatic processing [eis, 2005]. These new systems are already being used in a number of different ways including creating volumetric reconstructions of plasma parameters [Semeter *et al.*, 2009; Nicolls and Heinselman, 2007; Dahlgren *et al.*, 2012a, b].

These new systems differentiate themselves from dish antennas in a fundamental way. Instead of dwelling in a single beam or scanning along a prescribed direction, an electronically phased array can move to a different beam position within its field of view on a pulse by pulse basis. This yields a new flexibility to integrate not only along time but in space in an arbitrary direction and can relax the assumptions of stationarity for traditional dish antennas.

In order to take advantage of this new flexibility we will put forth the idea of the space-time ambiguity function. This concept extends the range ambiguity to all three spatial dimensions along with time. In the end this ambiguity can be represented as kernel in a Fredholm integral equation,

$$\rho(\mathbf{r}_s) = \int K(\mathbf{r}_s, \mathbf{r}) R(\mathbf{r}) d\mathbf{r} \quad (1)$$

where, for ISR, $R(\mathbf{r})$ is the lag of the autocorrelation function at a specific time and position.

By using this formulation many parallels between ISR and classic camera blurring problems can be made. In cameras blurring can take place when an object moves over a space covered by one pixel while the shutter is open and the CCD is collecting photons. A diagram of this can be seen in Figure 1. The same holds for ISR except that the pixels are no longer square and instead are determined by the beam shape and pulse pattern. This is shown in the diagrams in Figure 2.

In this publication we will describe a model for the full space-time ambiguity function for ISR systems. The impact of the three-dimensional ambiguity on moving plasma will be shown through specific cases related to the polar cap patches. A simulation of a polar cap patch using a full ISR simulator, which creates ISR data at the IQ level, will be shown. Lastly possible mitigation techniques will be explored. These mitigation techniques will borrow heavily from the image and signal processing literature.

2. Space-Time Ambiguity

The space-time ambiguity can be thought of as a kernel to a combined volume and time integration. As such definitions of space and time coordinates are needed.

First a three dimensional coordinate system is defined as $\mathbf{r} = [x, y, z]^T$. For this coordinate system, $\mathbf{r} = [0, 0, 0]^T$ at the location of the radar and thus $r = |\mathbf{r}|$, also known as the range variable. This allows for the use of polar coordinates $\mathbf{r} = [r, \theta, \phi]^T$ where θ is the physical elevation angle, ϕ is the physical azimuth angle.

The radar will sample this space into a set of discrete points which will be referred to as $\mathbf{r}_s = [x_s, y_s, z_s]^T$ along with the discretized range $r_s = |\mathbf{r}_s|$. The sampled space will consist of a number of points which are the combinations of range gates and number of beams. These points can also be referred in the polar coordinates $\mathbf{r}_s = [r_s, \theta_s, \phi_s]^T$, where θ_s is the sampled elevation angle, ϕ_s is the sampled azimuth angle.

For notation purposes we use two different sets of time commonly known in radar literature as fast-time, n and slow-time, t [Richards, 2005].. Fast-time is used to explore the workings of the radar on the order of the radar systems A/D conversion such as lag formation. Slow-time will be used for processes that vary in time on the order of the system's pulse repetition interval (PRI). In order to form estimates of the ACFs, with desired statistical properties, it is assumed that the plasma parameters will change on the order of 10's to hundreds of PRIs. The terms n and t will represent a continuous variables while n_s and t_s will be the fast time and slow time parameters sampled by the radar. The sampling rate of n_s will be the sampling rate of the A/D converters. The sampling of t_s can at the highest rate, be the PRI and at lowest, sampled once in a non-coherent processing interval (NCPI), or a period of time it takes the radar to average the desired number of pulses.

2.1. Derivation

107 The basic physical mechanism behind ISR is that electron density fluctuations in
 108 the ionosphere, $n_e(\mathbf{r}, n)$, scatter radio waves which can be observed by the receiver
 109 system of the radar [Dougherty and Farley, 1960]. The emitted radar signal at the
 110 transmitter will have a pulse shape $s(n)$ modulated at a central frequency that results
 111 in a scattering wave number \mathbf{k} . Using the Born approximation the signal received at
 112 time n , $x(n)$, can be represented as the following

$$x(n) = h(n) * \int e^{-j\mathbf{k}\cdot\mathbf{r}} s\left(n - \frac{2r}{c}\right) n_e(\mathbf{r}, n) d\mathbf{r}, \quad (2)$$

113 where $h(n)$ is the receiver filter and the $*$ represents the convolution operator. In
 114 modern ISR systems this signal $x(n)$ is then sampled at discrete points in fast-time
 115 which will be referred to as n_s . The convolution and sampling operation can be
 116 brought in the integral as the following,

$$x(n_s) = \int e^{-j\mathbf{k}\cdot\mathbf{r}} s\left(n - \frac{2r}{c}\right) n_e(\mathbf{r}, n) h(n_s - n) d\mathbf{r} dn \quad (3)$$

117 Once the signal has been received and sampled the autocorrelation function is
 118 then estimated from the sampled signal $x(n_s)$. The full expression of the underlying
 119 autocorrelation of this signal is the following,

$$\begin{aligned} \langle x(n_s) x^*(n'_s) \rangle &= \int e^{-j\mathbf{k}\cdot(\mathbf{r}'-\mathbf{r})} s\left(n - \frac{2r}{c}\right) s^*\left(n' - \frac{2r'}{c}\right) \\ &\quad h(n_s - n) h(n'_s - n') \langle n_e(\mathbf{r}, n) n_e^*(\mathbf{r}', n') \rangle d\mathbf{r} d\mathbf{r}' dn dn', \quad (4) \end{aligned}$$

where r' is the magnitude of the vector \mathbf{r}' . By assuming stationarity of second order signal statistics along fast time, we can then substitute the the lag variables $\tau \equiv n' - n$, and $\tau_s \equiv n'_s - n_s$. With these substitutions Equation 4 becomes

$$\langle x(n_s)x^*(n_s + \tau_s) \rangle = \int e^{-j\mathbf{k} \cdot (\mathbf{r}' - \mathbf{r})} s\left(n - \frac{2r}{c}\right) s^*\left(n + \tau - \frac{2r'}{c}\right) h(n_s - n)h(n_s + \tau_s - n - \tau) \langle n_e(\mathbf{r}, n)n_e^*(\mathbf{r}', n + \tau) \rangle d\mathbf{r}d\mathbf{r}'dn d\tau \quad (5)$$

We can make a simplifying assumption at this point that the space-time autocorrelation function of $n_e(\mathbf{r}, t)$, $\langle n_e(\mathbf{r}, n)n_e(\mathbf{r}', n + \tau) \rangle$, will go to zero as the magnitude of $\mathbf{x} \equiv \mathbf{r}' - \mathbf{r}$ increases. The rate that the space-time autocorrelation goes to zero will be such that $\tau \gg \frac{2\|\mathbf{x}\|}{c}$ thus in the argument of the pulse shape $r \approx r'$. This allows Equation 5 to be rewritten as

$$\langle x(n_s)x^*(n_s + \tau) \rangle = \int s\left(n - \frac{2r}{c}\right) s^*\left(n + \tau - \frac{2r}{c}\right) h(n_s - n)h^*(n_s + \tau_s - n - \tau) \left[\int e^{-2j\mathbf{k} \cdot \mathbf{x}} \langle n_e(\mathbf{r}, n)n_e^*(\mathbf{x} + \mathbf{r}, n + \tau) \rangle d\mathbf{x} \right] d\mathbf{r}dn d\tau. \quad (6)$$

The inner integral is a spatial Fourier transform evaluated at the wave number of the radar \mathbf{k} . By again asserting stationarity along slow time we can represent the true ACF as the following,

$$R(\tau, \mathbf{r}) = \langle |n_e(\mathbf{k}, r, \tau)|^2 \rangle \equiv \int_{\mathbf{x}} e^{-2j\mathbf{k} \cdot \mathbf{x}} \langle n_e(\mathbf{r}, b)n_e^*(\mathbf{x} + \mathbf{r}, n + \tau) \rangle d\mathbf{x}. \quad (7)$$

Now Equation 6 becomes

$$\langle x(n_s)x^*(n_s+\tau_s) \rangle = \int \langle |n_e(\tau, \mathbf{k}, \mathbf{r})|^2 \rangle \left[\int s\left(n - \frac{2r}{c}\right)s^*\left(n + \tau - \frac{2r}{c}\right)h(n_s - n)h^*(n_s + \tau_s - n - \tau)dn \right] d\tau dr. \quad (8)$$

If n_s is replaced with $2r_s/c$ we can introduce the range ambiguity function $W(\tau_s, r_s, \tau, r)$ by doing the following substitution,

$$W(\tau_s, r_s, \tau, r) = \int s\left(n - \frac{2r}{c}\right)s^*\left(n + \tau - \frac{2r}{c}\right)h(2r_s/c - n)h^*(2r_s/c + \tau_s - n - \tau)dn. \quad (9)$$

Assuming, for the moment, that $R(\tau, \mathbf{r})$ only varies across the range dimension r we can now represent this in the form of a Fredholm integral equation

$$\langle x(2r_s/c)x^*(2r_s/c + \tau_s) \rangle = \int W(\tau_s, r_s, \tau, r)R(\tau, r)drd\tau. \quad (10)$$

The range ambiguity function, $W(\tau_s, r_s, \tau, r)$, can be thought of as a smoothing operator along the range and lag dimensions of $R(\tau, r)$.

The spatial ambiguity across angle is determined by the antenna beam pattern. In phase array radars this beam pattern is ideally the array factor multiplied by the element pattern [Balanis, 2005]. The array factor is determined by a number of things including the element spacing in both x and y (dx, dy) and the wave number of the radar, k . Making idealized assumptions with no mutual coupling and that the array elements are cross dipole elements AMISR systems will have the following antenna pattern for pointing angle (θ_s, ϕ_s) ,

$$F(\theta_s, \phi_s, \theta, \phi) = \frac{1}{2}(1 + \cos(\theta)^2) \left[\frac{1}{MN} \left(1 + e^{j(\psi_y/2 + \psi_x)} \right) \frac{\sin((M/2)\psi_x)}{\sin(\psi_x)} \frac{\sin((N/2)\psi_x)}{\sin(\psi_x/2)} \right]^2, \quad (11)$$

where $\psi_x = -kd_x(\sin \theta \cos \phi - \sin \theta_s \cos \phi_s)$, $\psi_y = -kd_y(\sin \theta \sin \phi - \sin \theta_s \sin \phi_s)$ and M is the number of elements in the x direction of the array, and N is the number of elements in the y direction(see Appendix: A for derivation).

The spatial ambiguity is a separable function made up of the components of $W(\tau_s, \tau, r_s, r)$ and $F(\theta_s, \phi_s, \theta, \phi)$. These two functions can be combined by multiplying the two, creating the spatial ambiguity function $K(\tau_s, \mathbf{r}_s, \tau, \mathbf{r})$, and then doing a volume integration. This will create radar system's estimate of the ACF using one pulse which will be referred to as $\rho(\tau_s, \mathbf{r}_s)$,

$$\rho(\tau_s, \mathbf{r}_s) = \int F(\theta_s, \phi_s, \theta, \phi) W(\tau_s, r_s, \tau, r) R(\tau, \mathbf{r}) dV, \quad (12)$$

$$= \int K(\tau_s, \mathbf{r}_s, \tau, \mathbf{r}) R(\tau, \mathbf{r}) dV. \quad (13)$$

A rendering of an example of this full ambiguity function for an uncoded long pulse and antenna pattern in Equation 11 for four beams can be seen in Figure 3.

This one pulse is a single sample of a random process. In order to create a usable estimate multiple samples of this ACF need to be averaged together to reduce the variance to sufficient levels in order to fit the estimate to a theoretical ACF that is tied to plasma parameter values. To show the impact of this averaging to create the estimate of the ACF we will add slow-time dependence to $R(\tau, \mathbf{r}, t)$ along with another separable function $G(t_s, t)$ to the kernel. This function $G(t_s, t)$, while reducing the variance can create blurring of the ACF if the plasma parameters change with in a NCPI. Since the radar is sampling the space with individual pulses this function can take the form of a summation of Dirac delta functions

$$G(t_s, t) = \sum_{j=0}^{J-1} \alpha_j \delta(t - t_s - jT_{PRI}), \quad (14)$$

where J is the number of pulses used over a NCPI, T_{PRI} is the PRI time period and α_j is the weights that the radar assigns to the pulses. The weights are generally set to $1/J$ to simply average the pulses. With Equation 14 incorporated into the overall ambiguity we see the full integral equation,

$$\rho(\tau_s, \mathbf{r}_s, t_s) = \int G(t_s, t) K(\tau_s, \mathbf{r}_s, \tau, \mathbf{r}) R(\tau, \mathbf{r}, t) dV dt \quad (15)$$

$$\rho(\tau_s, \mathbf{r}_s, t_s) = \int L(\tau_s, \mathbf{r}_s, t_s, \tau, \mathbf{r}, t) R(\tau, \mathbf{r}, t) dV dt. \quad (16)$$

The final kernel, $L(\tau_s, \mathbf{r}_s, t_s, \tau, \mathbf{r}, t)$ encompasses the full space-time ambiguity.

2.2. Ambiguity after Frame Transformation

We will now focus on the impact of the motion of plasma as it is going through the field of view of the radar. We will assume that the radar is integrating over a length of time T beginning at t_s . The kernel L will be represented as a separable function K and G as in Equation 15. In this case G will be a summation of Dirac delta functions with weights of $1/J$. This will change Equation 15 to the following,

$$\rho(\tau_s, \mathbf{r}_s, t_s) = \int K(\tau_s, \mathbf{r}_s, \tau, \mathbf{r}) \left[(1/J) \int_{t_s}^{t_s+T} \sum_{j=0}^{J-1} \delta(t - t_s - jT_{PRI}) R(\tau, \mathbf{r}, t) dt \right] dV. \quad (17)$$

Of specific interest are instances in the high latitude ionosphere where embedded plasma structures are moving due to the electric field of the magnetosphere. Because

of this it will be assumed that the plasma is a rigid object and will not deform with respect to \mathbf{r} over time period $[t_0, t_0 + T]$ where $T = JT_{PRI}$ is the time for one NCPI. Also it will be assumed that it will be moving with a constant velocity \mathbf{v} . Thus $R(\tau, \mathbf{r}, t) \Rightarrow R(\tau, \mathbf{r} + \mathbf{v}t)$. The assumption of rigidity is possible to make over the time period of the NCPI, on the order of a few minutes, while the plasma moves through the field of view of the radar. One example can be taken from the high latitude ionosphere while large scale features in structures such as patches decay on the order of hours [Tsunoda, 1988]. This assumption is useful because it shows the utility of this frame work to analyze the impacts on the true resolution of the ISR systems. With these assumption Equation 17 becomes,

$$\rho(\tau_s, \mathbf{r}_s, t_s) = (1/J) \int_{t_s}^{t_s+T} \sum_{j=0}^{J-1} \delta(t - t_s - jT_{PRI}) K(\tau_s, \mathbf{r}_s, \tau, \mathbf{r}) R(\tau, \mathbf{r} + \mathbf{v}t) dt dV \quad (18)$$

A change of variables to $\mathbf{r}' = \mathbf{r} + \mathbf{v}t$ acts as a Galilean transform and applies a warping to the kernel, changing the frame of reference. Since $R(\tau, \mathbf{r}')$ is no longer dependent on t Equation 18 becomes,

$$\rho(\tau_s, \mathbf{r}_s, t_s) = (1/J) \int \left[\sum_{j=0}^{J-1} K(\tau_s, \mathbf{r}_s, \tau, \mathbf{r}' - \mathbf{v}(t_s + jT_{PRI})) \right] R(\tau, \mathbf{r}') dV. \quad (19)$$

By performing the integration in t the problem can now be simplified further back to a Fredholm integral equation by simply replacing the terms in the square brackets as a new kernel $A(\tau_s, \mathbf{r}_s, t_s, \tau, \mathbf{r}')$,

$$\rho(\tau_s, \mathbf{r}_s, t_s) = \int A(\tau_s, \mathbf{r}_s, t_s, \tau, \mathbf{r}') R(\tau, \mathbf{r}') dV. \quad (20)$$

The impact of the plasma velocity on the ambiguity function can be seen in Figure 4. This is the same ambiguity as seen in Figure 3 but with a velocity of 500 m/s in the y direction over a period of 2 minutes. This velocity creates a larger ambiguity function in the frame of reference of the moving plasma.

The operator A can be determined through knowledge of the radar system's beam pattern along with the experiments pulse pattern, integration time and velocity of the plasma. This velocity \mathbf{v} can be estimated by taking measurements of the Doppler shift and using a methodology seen in [Butler et al., 2010]. Once the operator has been determined standard processing techniques can be used as if the plasma is not moving, under the previous assumptions.

3. Simulation

In order to show the impact of the ambiguity function, synthetic data was created using a known condition of a simulated ionosphere. The simulator creates data by deriving time filters from the autocorrelation function and applying them to complex white Gaussian noise generators. Stating this in another way, every point in time and space has a noise plant and filter structure as in Figure 5. The data is then scaled and summed together according to its location in range and angle space to radar.

After the IQ data has been created it is processed to create estimates of the ACF at desired points of space. This processing follows a flow chart seen in Figure 6.

The sampled I/Q can be represented as $x(n) \in \mathbb{C}^N$ where N is the number of samples in an inter pulse period. At this point the first step in estimating the autocorrelation function is taken. For each range gate $m \in 0, 1, \dots, M-1$ an autocorrelation is estimated for each lag of $l \in 0, 1, \dots, L-1$. To get better statistics this operation is performed for each pulse $j \in 0, 1, \dots, J-1$ and then summed over the J pulses. The entire operation to form the initial estimate of $\hat{R}(m, l)$ is the following,

$$\hat{R}(m, l) = \sum_{j=0}^{J-1} x(m - \lfloor l/2 \rfloor, j) x^*(m + \lceil l/2 \rceil, j). \quad (21)$$

The case shown in Equation 21 is a centered lag product, other types of lag products calculations are available but generally a centered product is used. In the centered lag product case range gate index m and sample index n can be related by $m = n - \lfloor L/2 \rfloor$ and the maximum lag and sample relation is $M = N - \lceil L/2 \rceil$.

After the lag products have been formed an estimate of the noise correlation is subtracted out of $\hat{R}(m, l)$, which is defined as $\hat{R}_w(m, l)$,

$$\hat{R}_w(m_w, l) = \sum_{j=0}^{J-1} w(m_w - \lfloor l/2 \rfloor, j) w^*(m_w + \lceil l/2 \rceil, j), \quad (22)$$

where $w(n_w)$ is the background noise process of the radar. Often the noise process is sampled during a calibration period for the radar when nothing is being emitted. The final estimate of the autocorrelation function after the noise subtraction and summation rule will be represented by $\hat{R}_f(m, l)$. At this point a summation rule is applied and the data is sent off to be fit.

In order to demonstrate the blurring taking place from the motion of plasma a phantom ionosphere is created where a small plasma enhancement moves through the radar field of view. The background electron density varies in altitude as a Chapman function while the electron and ion temperature remains constant. This can be seen in Figure 7. This is done to avoid having to do full fit and thus only try to measure the electron density. Also estimates of the zeroth lag are only necessary. Added to this is a 35 km radius sphere of enhance electron density of about $5 \times 10^{10} \text{ m}^{-3}$ centered at 400 km altitude moving at 500 m/s along the \mathbf{y} direction. Images from this phantom can be seen in Figure 8.

Using the phantom we can see how just simply changing the integration time can impact the reconstruction. In Figure 10 we can see a case were only 10 pulses are used for the reconstruction. This corresponds to an integration time of about 9 seconds using the 121 beam pattern which can be seen in Figure 9. The enhancement can be seen with concentrated energy as it moves through the field of view. The problem is that there is a high amount of variance in the reconstruction. Figure 11 shows the reconstruction with 200 pulses, 3 minute integration time. The variability has been reduced but there is a large amount of blurring of the enhancement as it moves through the field of view.

In order to give a comparison a phantom was also created with no motion. This can be seen in first pane Figure 12. An image using the same integration time as in Figure 10 for the stationary phantom is the center pane in Figure 12. Another

image using the longer integration time can be seen in right pane of Figure 12. These images show that the blurring is on the same order between both integration times.

Lastly we show results of a simulation of the plasma density enhancement through the field of view with full fitting. We again use a plasma enhancement moving through the field of view at 500 m/s but the electron and ion temperature varies with time and altitude. The background ion and electron temperature vs. height can be seen in Figure 14. As the electron density enhancement travels through the field of view the temperatures drop by the same ratio that the electron density is enhanced.

The phantoms for each parameter at approximately 402 seconds can be seen in Figure 14. The reconstruction of this field at the same time can be seen in Figure 15. The reconstruction does not seem to show the electron density enhancement even in a blurred form. This is likely due to the nonlinear nature of the fitting.

4. Possible Mitigation Techniques

There are a number of possible ways to remove the ISR operator function to the data. A relatively simply way to remove the problem is to process the data in the frame of reference of the plasma. Already it has been shown that it is possible to measure the vector velocity of plasma flows, [Butler *et al.*, 2010]. After measuring the velocity instead of integrating in the same beam one could integrate across different beams using this knowledge. This would allow for ACF to be formed from the same populations of plasma as it moves through the field of view.

In order to reconstruct the plasma parameters it is necessary to do some sort of regularization. There are two type of regularization that can be applied in this case the first is parameter based regularization, like full profile analysis, and the other is data based regularization. The term parameter based regularization in this case means applying constraints to the physical parameters that are often determined after fitting. This requires a large amount of calculation because the fitting and constraints are done in one step. Currently full profile analysis has only been applied along the range dimension and not in all three spatial dimensions. Extending this to three dimensions may make these algorithms computationally infeasible.

Data based regularization infers the application of constraints to the estimates of the autocorrelation functions. The constraints usually deal with how the data changes over time and space by constraining the energy of the ACFs or its derivative. This has an advantage of being more computationally tractable in that it is now a linear inverse problem. Using the ideas stated in this paper one can cast the reconstruction of the four dimensional function of the ACFs in these terms. The issue with doing this data based reconstruction is it is unknown how to constrain the reconstruction in the best way.

The two examples of data based regularization in the one dimensions ISR literature are lag profile inversion and deconvolution methods. Lag profile inversion creates an operator that takes the measured data from a theoretical ACFs to the measured ACFs [Virtanen *et al.*, 2008]. Along with the operator there is also an assumed Gaussian error. This error can be then estimated from the data. This Bayesian frame work can

actually be rewritten as a least squares minimization along with a Tikhonov constraint.

Because of this one can show that the deconvolution methods from *Nikoukar et al.* [2008] have almost the same structure as lag profile inversion.

With this in mind one can go a step further and investigate super resolution methods seen in image processing literature [*Takeda et al.*, 2009],[*Takeda and Milanfar*, 2011]. With these techniques along with the data regularization based framework in one dimensional ISR these techniques could be used to reconstruct the ACFs. This would require a complete change in the methodology in which 3-D ISR data is investigated. Basically instead of fitting data in the coordinate space of the radar we would first re-grid the data in a Cartesian space and then apply the nonlinear fitting. This would have the advantage of working with a linear inverse problem but the issues would be the same as with other data based regularization techniques were there is a question of what type of constraint should be used as opposed to a straight forward physical constraint.

5. Conclusion

We have presented a new method for analyzing incoherent scatter radar processing through use of the full space-time ambiguity function. This allows for taking into account the antenna beam pattern, pulse pattern and time integration. Through simulation we have shown how plasma motion can impact reconstruction of parameters which compounded with the non-linear nature of the parameter fitting step can create errors which are hard to predict. Lastly we have suggested a number of ways

using three dimensional ISR systems we could mitigate these errors and reconstruct parameters at higher resolutions than what is currently possible.

Appendix A: Derivation of Idealized AMISR Array Pattern

The current antenna on the AMISR systems is made up 8x16 set of panel of half wave cross dipoles. Each panel has 32 cross dipoles in a 8x4 hexagonal configuration. In the current set up at the Poker Flat site this yields at 4096 element array in a 64x64 element hexagonal configuration.

In order to simplify the antenna can be treated as two rectangular arrays of cross dipoles interleaved together. In the x direction each of these arrays will have a spacing of $2d_x$ with $M/2$ elements. The y direction will be of length N elements and spacing d_y . Using basic planar phase array theory, [Balanis, 2005], we can start with the linear array pattern from the first array can be represented as

$$E_1(\theta, \phi) = \sum_{m=1}^{M/2} \sum_{n=1}^N e^{-j2(m-1)kd_x \sin \theta \cos \phi - j(n-1)kd_y \sin \theta \sin \phi}. \quad (\text{A1})$$

Since the second array can be thought of a shifted version of the first in the x direction we get the following

$$E_2(\theta, \phi) = \sum_{m=1}^{M/2} \sum_{n=1}^N e^{-j(2m-1)kd_x \sin \theta \cos \phi - j(n-1/2)kd_y \sin \theta \sin \phi}. \quad (\text{A2})$$

In order to simplify notation we will make the following substitutions, $\psi_x = -kd_x \sin \theta \cos \phi$, $\psi_y = -kd_y \sin \theta \sin \phi$. Using Equations A1 and A2 we can see the following relationship,

$$E_2(\theta, \phi) = e^{j(\psi_y/2 + \psi_x)} E_1(\theta, \phi) = \sum_{m=1}^{M/2} \sum_{n=1}^N e^{-j2(m-1)\psi_x - j(n-1)\psi_y}. \quad (\text{A3})$$

313 Adding E_1 and E_2 together we get the following linear array pattern

$$\begin{aligned} E(\theta, \phi) &= (1 + e^{j(\psi_y/2 + \psi_x)}) \sum_{m=1}^{M/2} \sum_{n=1}^N e^{-j2(m-1)\psi_x - j(n-1)\psi_y}. \\ &= \frac{1}{MN} (1 + e^{j(\psi_y/2 + \psi_x)}) \frac{\sin((M/2)\psi_x)}{\sin(\psi_x/2)} \frac{\sin((N/2)\psi_y)}{\sin(\psi_y/2)}. \end{aligned} \quad (\text{A4})$$

314 Since the array is steerable this can be taken into account in the equations by
 315 simply changing the definitions of ψ_x and ψ_y to $\psi_x = kd_x(\sin \theta \cos \phi - \sin \theta_s \cos \phi_s)$,
 316 and $\psi_y = kd_y(\sin \theta \sin \phi - \sin \theta_s \sin \phi_s)$. Lastly the antenna pattern of a single cross
 317 dipole can be represented as $\frac{1}{2}(1 + \cos^2(\theta))$ [Balanis, 2005]. By taking the squared
 318 magnitude of the array factor and multiplying it with the pattern of the dipole we
 319 get Equation 11,

$$F(\theta_s, \phi_s, \theta, \phi) = \frac{1}{2}(1 + \cos^2(\theta)) \left| \frac{1}{MN} (1 + e^{j(\psi_y/2 + \psi_x)}) \frac{\sin((M/2)\psi_x)}{\sin(\psi_x/2)} \frac{\sin((N/2)\psi_y)}{\sin(\psi_y/2)} \right|^2. \quad (\text{A5})$$

References

- 320 (2005), Eiscat 3d design specification document.
- 321 (2014), Amisr overview.
- 322 Balanis, C. A. (2005), *Antenna Theory: Analysis and Design*, Wiley-Interscience.
- 323 Butler, T. W., J. Semeter, C. J. Heinselman, and M. J. Nicolls (2010), Imaging f
- 324 region drifts using monostatic phased-array incoherent scatter radar, *Radio Sci.*,

- 325 45(5), RS5013, doi:10.1029/2010RS004364.
- 326 Dahlgren, H., J. L. Semeter, K. Hosokawa, M. J. Nicolls, T. W. Butler, M. G. Johnsen,
327 K. Shiokawa, and C. Heinselman (2012a), Direct three-dimensional imaging of polar
328 ionospheric structures with the resolute bay incoherent scatter radar, *Geophysical*
329 *Research Letters*, 39(5), n/a–n/a, doi:10.1029/2012GL050895.
- 330 Dahlgren, H., G. W. Perry, J. L. Semeter, J. P. St. Maurice, K. Hosokawa,
331 M. J. Nicolls, M. Greffen, K. Shiokawa, and C. Heinselman (2012b), Space-
332 time variability of polar cap patches: Direct evidence for internal plasma struc-
333 turing, *Journal of Geophysical Research: Space Physics*, 117(A9), A09,312, doi:
334 10.1029/2012JA017961.
- 335 Dougherty, J. P., and D. T. Farley (1960), A theory of incoherent scattering of
336 radio waves by a plasma, *Proceedings of the Royal Society of London. Series A,*
337 *Mathematical and Physical Sciences*, 259(1296), pp. 79–99.
- 338 Dougherty, J. P., and D. T. Farley (1963), A theory of incoherent scattering of radio
339 waves by a plasma, 3 scattering in a partly ionized gas, *Journal of Geophysical*
340 *Research*, 68, 5473.
- 341 Farley, D. T., J. P. Dougherty, and D. W. Barron (1961), A theory of incoherent
342 scattering of radio waves by a plasma ii. scattering in a magnetic field, *Proceedings*
343 *of the Royal Society of London. Series A, Mathematical and Physical Sciences*,
344 263(1313), pp. 238–258.
- 345 Hagfors, T. (1961), Density fluctuations in a plasma in a magnetic field, with ap-
346 plications to the ionosphere, *Journal of Geophysical Research*, 66(6), 1699–1712,

doi:10.1029/JZ066i006p01699.

Lehtinen, M. S., and A. Huuskonen (1996), General incoherent scatter analysis and {GUISDAP}, *Journal of Atmospheric and Terrestrial Physics*, 58(1–4), 435 – 452, doi:http://dx.doi.org/10.1016/0021-9169(95)00047-X, Selected papers from the sixth international Eiscat Workshop.

Nicolls, M. J., and C. J. Heinselman (2007), Three-dimensional measurements of traveling ionospheric disturbances with the Poker Flat Incoherent Scatter Radar, *Geophysical Research Letters*.

Nikoukar, R., F. Kamalabadi, E. Kudeki, and M. Sulzer (2008), An efficient near-optimal approach to incoherent scatter radar parameter estimation, *Radio Science*, 43(5), n/a–n/a, doi:10.1029/2007RS003724.

Richards, M. A. (2005), *Fundamentals of Radar Signal Processing*, McGraw-Hill.

Semeter, J., T. Butler, C. Heinselman, M. Nicolls, J. Kelly, and D. Hampton (2009), Volumetric imaging of the auroral ionosphere: Initial results from pfisr, *Journal of Atmospheric and Solar-Terrestrial Physics*, 71, 738 – 743, doi:10.1016/j.jastp.2008.08.014, Advances in high latitude upper atmospheric science with the Poker Flat Incoherent Scatter Radar (PFISR).

Takeda, H., and P. Milanfar (2011), Removing Motion Blur With Space-Time Processing, *Image Processing, IEEE Transactions on*, 20(10), 2990–3000.

Takeda, H., P. Milanfar, M. Protter, and M. Elad (2009), Super-Resolution Without Explicit Subpixel Motion Estimation, *Image Processing, IEEE Transactions on*, 18(9), 1958–1975.

- 369 Tsunoda, R. T. (1988), High-latitude F region irregularities: A review and synthesis,
370 *Reviews of Geophysics*.
- 371 Virtanen, I. I., M. S. Lehtinen, and T. Nygrén (2008), Lag profile inversion method
372 for EISCAT data analysis, *Annales . . .*
- 373 Zesta, E., E. Donovan, L. Lyons, G. Enno, J. S. Murphree, and L. Cogger (2002),
374 Two-dimensional structure of auroral poleward boundary intensifications, *Jour-*
375 *nal of Geophysical Research: Space Physics*, 107(A11), SIA 6–1–SIA 6–20, doi:
376 10.1029/2001JA000260.
- 377 Zesta, E., L. Lyons, C.-P. Wang, E. Donovan, H. Frey, and T. Nagai (2006), Auroral
378 poleward boundary intensifications (pbis): Their two-dimensional structure and
379 associated dynamics in the plasma sheet, *Journal of Geophysical Research: Space*
380 *Physics*, 111(A5), n/a–n/a, doi:10.1029/2004JA010640.

381 **Acknowledgments.** (Text here)

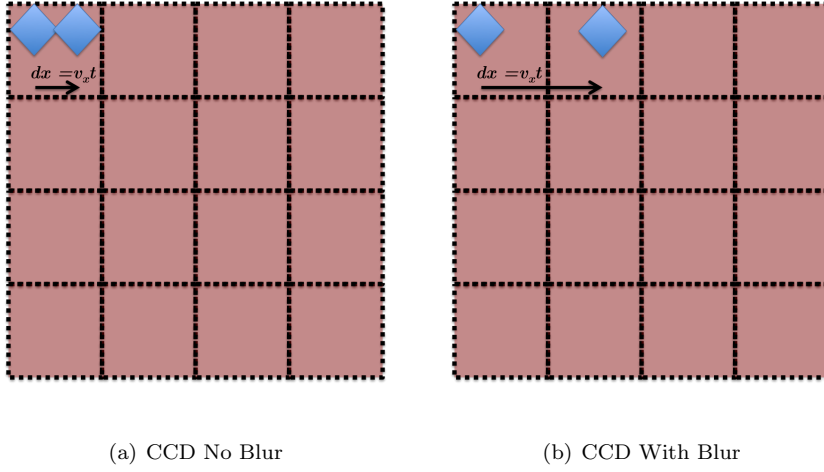


Figure 1. CCD camera

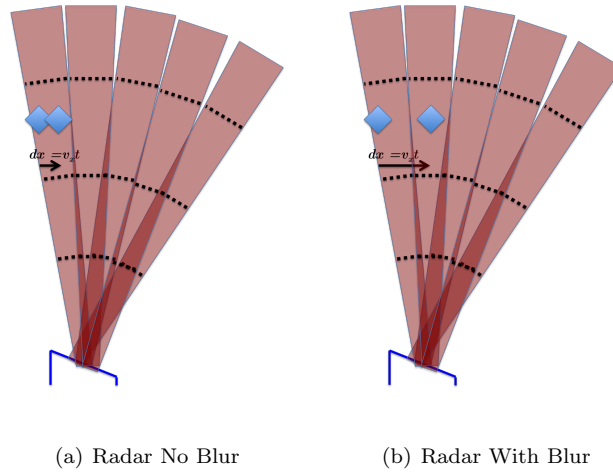


Figure 2. Radar

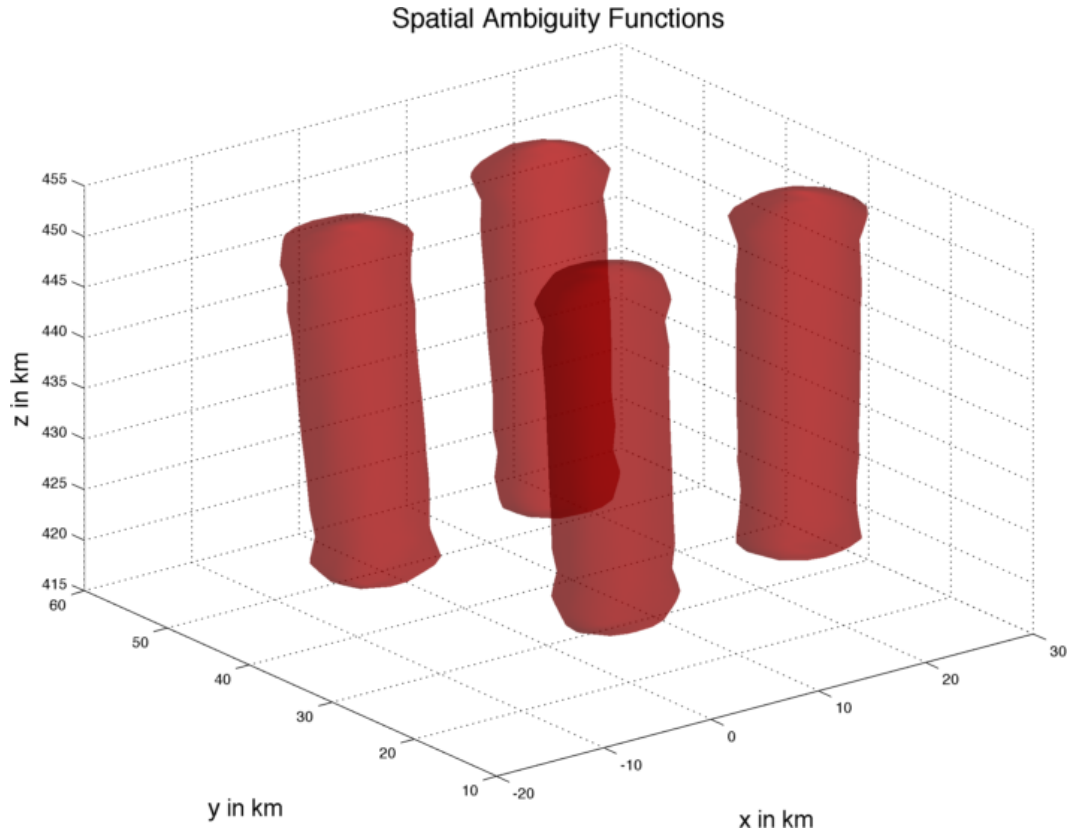


Figure 3. Full Spatial Ambiguity Function

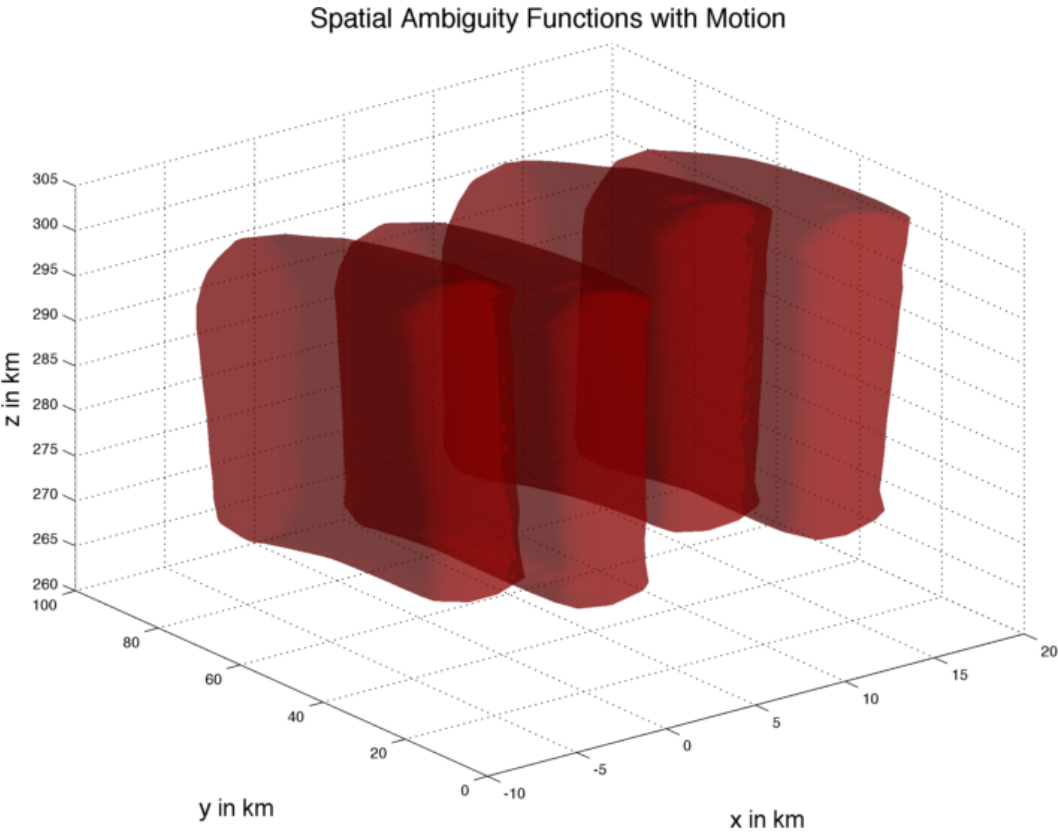


Figure 4. Full Spatial Ambiguity Function With Motion

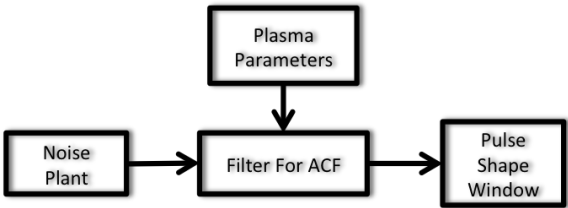


Figure 5. I/Q Simulator Diagram

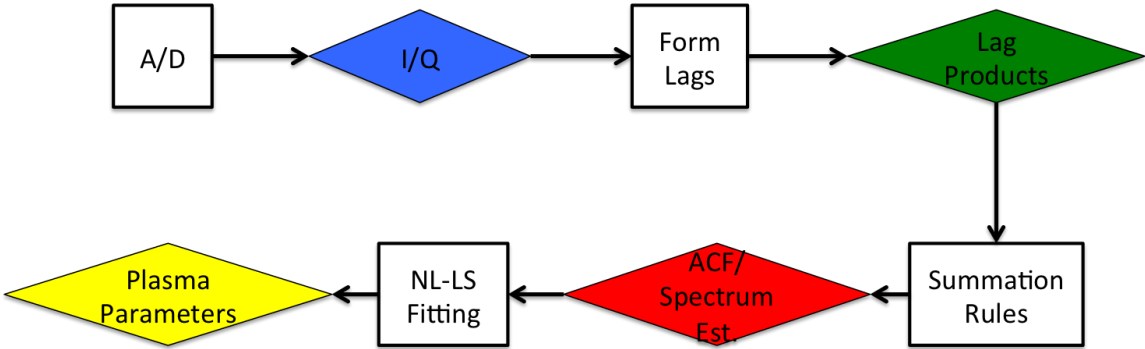


Figure 6. ISR Processing Chain.

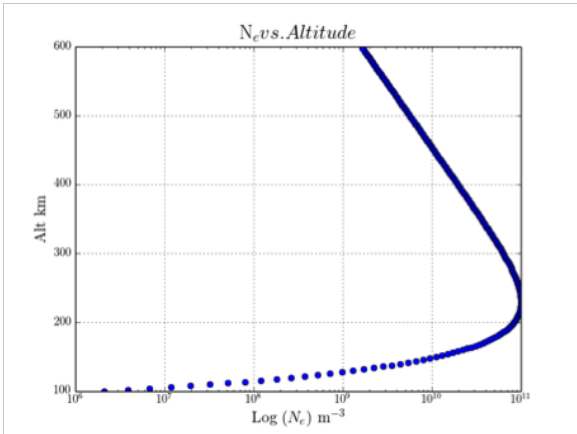


Figure 7. Electron density vs. altitude.

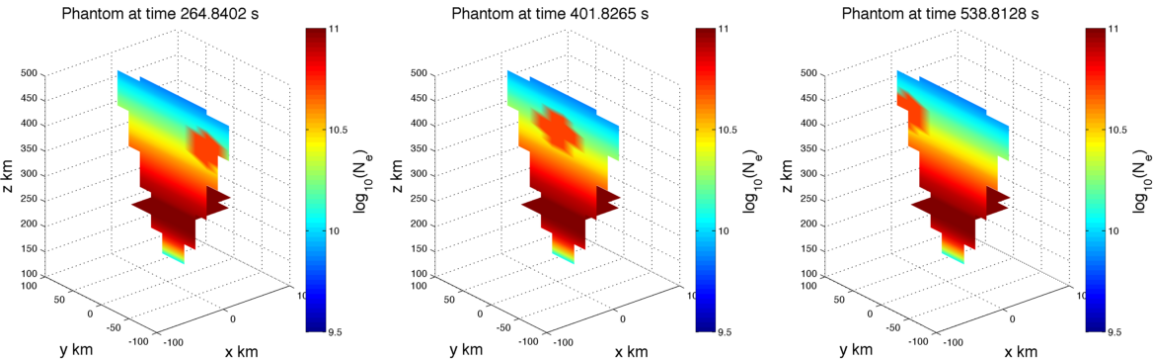


Figure 8. Example images from phantom

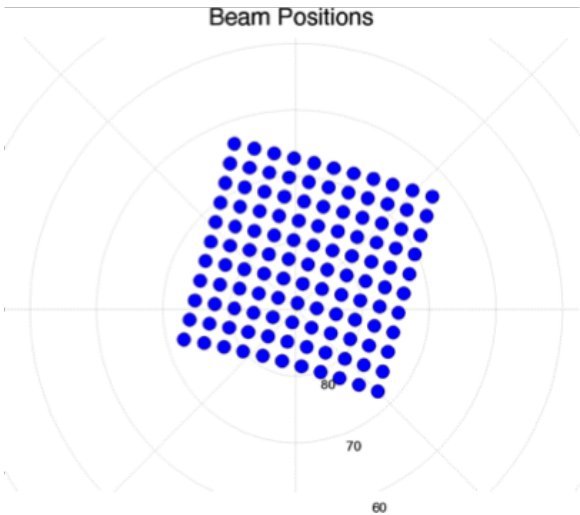


Figure 9. Beam pattern

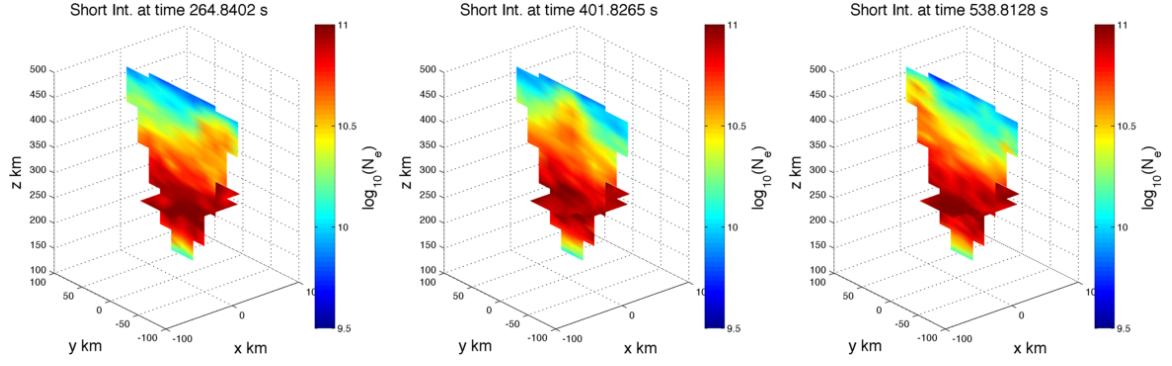


Figure 10. Example images from variable data

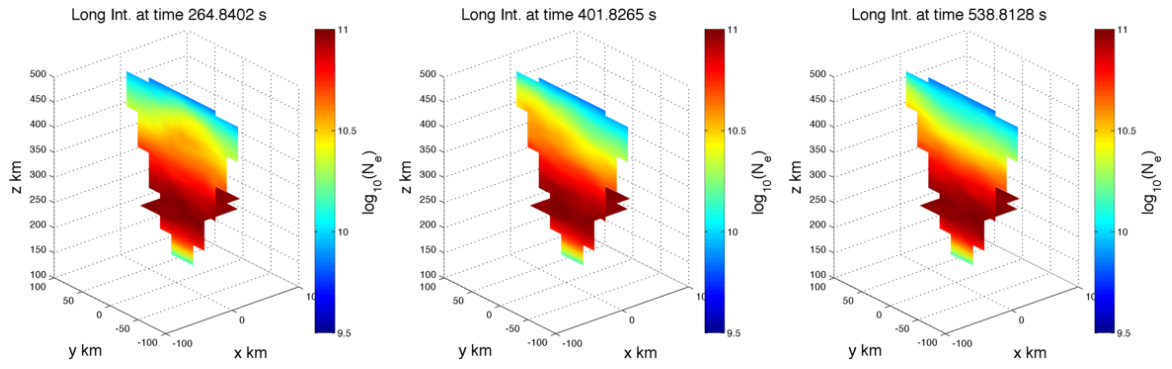


Figure 11. Example images from blurred data

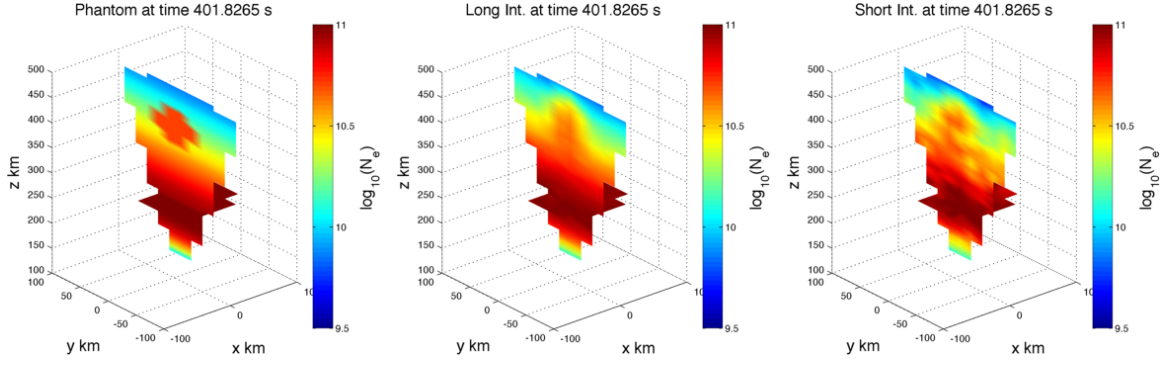


Figure 12. Stationary phantom along with both types of reconstructions.

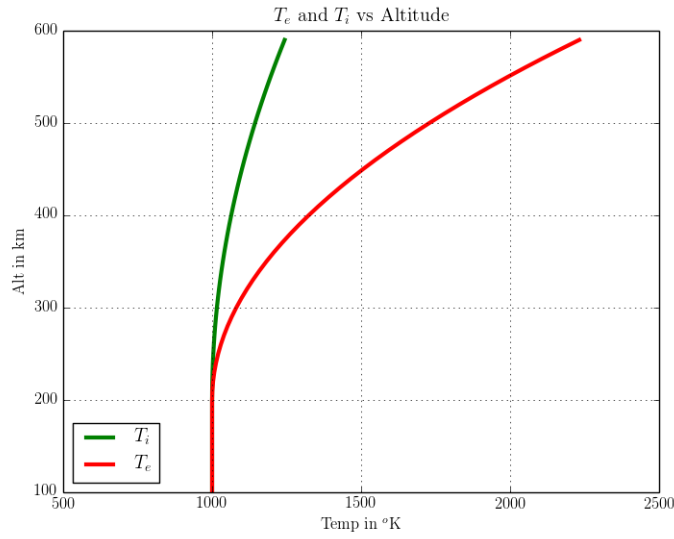


Figure 13. Ion & electron temperature vs. height.

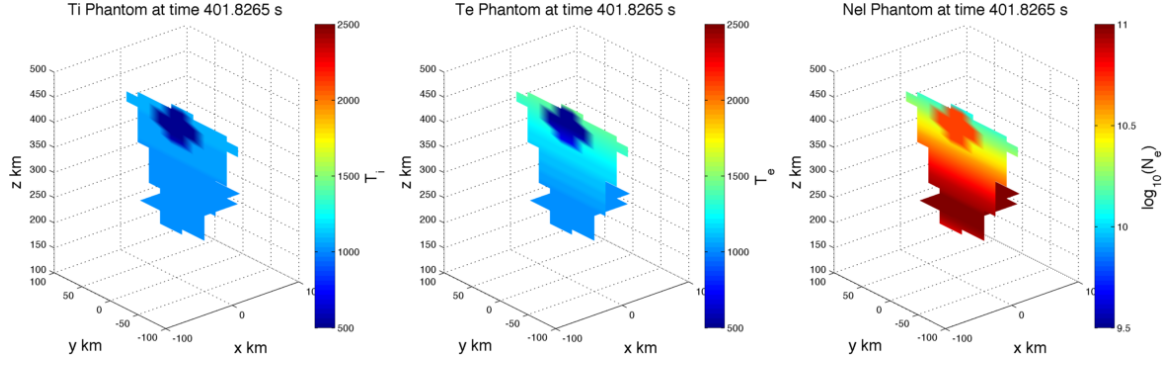


Figure 14. Phantom of parameters.

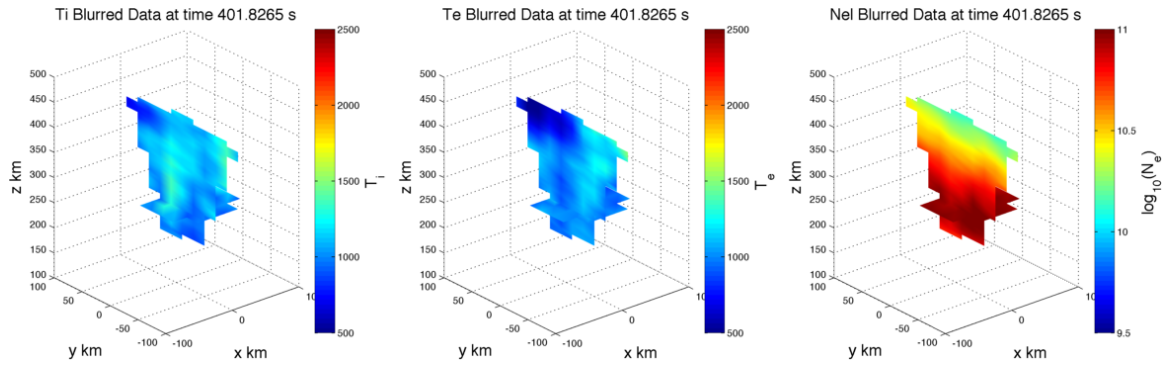


Figure 15. Blurred data after full fitting.